

Article

# Sonochemical Synthesis of Ce-doped TiO<sub>2</sub> Nanostructure: A Visible-Light-Driven Photocatalyst for Degradation of Toluene and O-Xylene

Joon Yeob Lee <sup>1</sup> and Jeong-Hak Choi <sup>2,\*</sup><sup>1</sup> Life Environmental R&D Center, CHEMTOPIA Co., Ltd., Seoul 08377, Korea; jlee@chemtopia.net<sup>2</sup> Department of Environmental Engineering, Catholic University of Pusan, Busan 46252, Korea;

\* Correspondence: jhchoi@cup.ac.kr; Tel.: +82-51-510-0637; Fax: +82-51-510-0628

Received: 20 March 2019; Accepted: 17 April 2019; Published: 17 April 2019



**Abstract:** Ce-doped TiO<sub>2</sub> nanostructures (CeT) with different amounts of Ce (0.5, 0.75, 1.0, 1.5, and 2.0 wt. %) were synthesized using a sonochemical processing method. The physicochemical properties of the prepared samples were explored using UV-visible diffuse reflectance spectroscopy (UV-vis DRS), field-emission TEM (FE-TEM), XRD, X-ray photoelectron spectroscopy (XPS), photoluminescence spectroscopy (PL), and surface area and pore size analyzers. The photocatalytic performance of the prepared CeT was assessed by monitoring their degradation efficiencies for gaseous toluene and o-xylene—widely known as significant indoor air pollutants—under daylight irradiation. The prepared CeT exhibited significantly improved photocatalytic performance towards the degradation of toluene and o-xylene, which was much higher than that observed for pure TiO<sub>2</sub> and commercial P25 TiO<sub>2</sub>. Particularly, photocatalytic degradation efficiencies by the prepared CeT catalysts increased remarkably in the case of o-xylene (up to 99.4%) compared to toluene (up to 49.1%). The degradation efficiency by the CeT was greatest for the CeT-0.75 sample, followed by, in order, CeT-1.0, CeT-0.5, CeT-1.5, and CeT-2.0 samples in agreement with the order of the surface area and the particle size of the catalysts. According to the change of light source, the average decomposition efficiencies for toluene and o-xylene by CeT-0.75 were shown in the order of conventional daylight lamp > violet light emitting diodes (LEDs) > white LEDs. The decomposition efficiencies normalized to supplied electric power, however, were estimated to be in the following order of violet LEDs > white LEDs > conventional daylight lamp, indicating that the LEDs could be a much more energy efficient light source for the photodecomposition of target toluene and o-xylene using the CeT-0.75 photocatalyst.

**Keywords:** sonochemical processing method; Ce content; light sources; photocatalyst

## 1. Introduction

Aromatic volatile compounds are considered to be serious indoor air pollutants because they can cause adverse health risks for building occupants [1]. The appearance of these compounds indoors results mainly from the wide use of them as building interior materials, household products, and so on [1]. Most aromatic volatile compounds are known for their carcinogenic effects, and in some cases, they can seriously damage the functioning of kidneys, liver, the respiratory system, and the central nervous system of human beings [2]. Actually, it has been reported that the central nervous system (CNS) is likely to be damaged by the exposure to toluene and xylene [3]. Exposure to low to moderate levels of toluene vapor can cause dizziness, nausea, confusion, memory loss, weakness, loss of appetite, hearing, and color vision loss. Long-term exposure to toluene vapors may lead to damage of the central nervous, the reproductive, and the immune systems, and can even cause death [3,4].

Inhaling xylene vapor can also lead to nausea, dizziness, headache, vomiting, loss of consciousness, damage of the central nervous system, and death [5]. Moreover, because a lot of people spend most of their time in indoor environments, the concentration level of these indoor air pollutants should be reduced to minimize the health risks of building occupants.

During the last few decades, titanium dioxide (TiO<sub>2</sub>) has received particular attention in the field of the photocatalytic elimination of various air and water contaminants [6–8] due to its effective properties such as non-toxicity, low cost, high resistance to photo-corrosion, and good physical and chemical stabilities [9–11]. However, bare TiO<sub>2</sub> has several drawbacks, including a wide band gap (~3.2 eV), which induces it as active only under UV light illumination ( $\lambda < 380$  nm) [12]—the undesirable recombination of photoexcited charge carriers in TiO<sub>2</sub> that results in a low photo quantum yield [11–13]. Thus, it is necessary to tune the band structure of TiO<sub>2</sub> to exhibit satisfactory photocatalytic reactivity under a broad range of solar spectrum including visible range as well as UV range. Moreover, reducing the frequency of the recombination of photoexcited electrons and holes is also essential to improving the photocatalytic performance of TiO<sub>2</sub>. Many strategies have attempted to address the mentioned drawbacks of TiO<sub>2</sub>, including dye sensitization, semiconductor compounding, and ion-doping [14–17]. In general, doping or incorporation of metal-ions into the TiO<sub>2</sub> structure is considered to be one of the highly applicable ways to develop novel TiO<sub>2</sub> catalysts [18]. In principle, the incorporation of metal ions can decrease the band-gap energy and therefore allow the photocatalytic activity of TiO<sub>2</sub> to expand to visible range [19–21]. Additionally, the metal dopants can capture the photoexcited electrons and hamper the charge-carrier recombination by accelerating charge transfer processes [22–24]. For these reasons, it is expected that the metal-doped TiO<sub>2</sub> can work more effectively in decomposing environmental pollutants than the pure TiO<sub>2</sub> [25,26].

In general, rare earth metal ions are known to be ideal dopants for tuning the electronic and crystal structures and light-harvesting characteristics of TiO<sub>2</sub> compared to various other metal ions because of the interaction between their *f*-orbital and the functional groups of organic compounds resulting in the formation of complexes with numerous Lewis bases such as thiols, alcohols, aldehydes, and organic acids [27,28]. Among the available rare earth metal ions, relatively non-toxic and inexpensive cerium (Ce) [29] has attracted more interest as a dopant because of the following reasons: (1) the distinct electronic structures between Ce<sup>4+</sup> (4f<sup>0</sup>5d<sup>0</sup>) and Ce<sup>3+</sup> (4f<sup>1</sup>5d<sup>0</sup>) can result in different optical and catalytic properties; (2) the redox couple Ce<sup>3+</sup>/Ce<sup>4+</sup> leads cerium oxide to shift between CeO<sub>2</sub> and Ce<sub>2</sub>O<sub>3</sub> under oxidizing and reducing conditions [30,31].

Additionally, various methods including sol-gel [32], hydrothermal [33], microwave [34], and sonochemical [35] were employed to prepare titania nanomaterials. Recently, ultrasonic synthesis has been used to prepare a variety of nano-structured catalysts in an aqueous solution, including TiO<sub>2</sub> [35], WO<sub>3</sub> [36], and ZnO [37]. A powerful driving force for this technique is transiently formed thermodynamics of hotspots during the formation/collapse of the ultrasonic cavitation bubbles, which reach a temperature of about 5000–25,000 K, a high pressure of about 20 Mpa, and heating/cooling rates above 10<sup>10</sup> K s<sup>-1</sup> [35–37]. Therefore, high temperature and pressures can lead to changes in the morphology of nanoparticles during ultrasonic treatment.

Therefore, in this study, Ce-doped TiO<sub>2</sub> (CeT) nanostructures with different amounts of Ce metal ions were synthesized via a sonochemical method known as an excellent and facile route for the fabrication of diverse nano-structured materials [38–40]. The fabricated samples were characterized and assessed for the degradation of gaseous toluene and o-xylene under daylight irradiation. The photocatalytic performance of the synthesized CeT was also compared with pure TiO<sub>2</sub> (PT) and commercial Degussa TiO<sub>2</sub> (P25). Moreover, two types of light emitting diodes (LEDs) were tested as light sources to compare the effects of the light source on the photodegradation performance, and the energy efficiencies of them were also evaluated.

## 2. Materials and Methods

### 2.1. Preparation of Pure TiO<sub>2</sub> and Ce-doped TiO<sub>2</sub> Nanostructures

The Ce-doped TiO<sub>2</sub> photocatalyst was synthesized by an ultrasonic treatment followed by a calcination process. Cerium nitrate hexahydrate (99%, Sigma–Aldrich, Saint Louis, MO, USA) was used as a source of Ce metal. The different amounts of Ce metal sources determined to provide metal to TiO<sub>2</sub> weight ratios of 0.5%, 0.75%, 1.0%, 1.5%, and 2.0%, respectively (denoted here as CeT-x, where x = Ce to TiO<sub>2</sub> wt. %) and 0.5 g of surfactant P-123 (Sigma–Aldrich) were dissolved in deionized water (100 mL) under vigorous stirring. Then, 25 mL of titanium tetraisopropoxide (99.9%, Sigma–Aldrich) was added dropwise into the above solution for about 3 min with magnetic stirring. The resulting solution was subjected to ultrasonic treatment for 60 min (Sonics & Materials VCX750, operating at an amplitude of 29 μm and a frequency of 20 kHz) and was then aged for 12 h. Subsequently, the obtained product in the mixture was separated by centrifugation (5000 rpm), washed with water, and then dried at 80 °C for 12 h in an electric dry oven. The final powder was calcined in an electric furnace at 500 °C for 1 h to get the CeT powder. Bare TiO<sub>2</sub> was also prepared using this procedure without adding Ce metal.

### 2.2. Characterization

The properties of the prepared photocatalysts were characterized using XRD (D/max-2500 diffractometer, Rigaku Corp., Tokyo, Japan), XPS (Quantera SXM, ULVAC-PHI, Inc., Chigasaki, Japan), UV-vis diffuse reflectance spectroscopy (UV-vis DRS) (CARY 5G, Varian, Palo Alto, CA, USA), field-emission TEM (FE-TEM) (Titan G2 ChemiSTEM (Cs probe), FEI Company, Hillsboro, OR, USA), photoluminescence spectroscopy (PL) (SpectraPro 2150i, Acton Research, Lakewood Ranch, FL, USA), and surface area and pore size analyzers (Autosorb-iQ & Quadrasorb SI, Quantachrome Instruments, Boynton Beach, FL, USA).

### 2.3. Photocatalytic Reactor System and Degradation of Target Compounds

The photocatalytic degradation experiments were conducted using a homemade reactor system similar to that used in our previous work [41], which is displayed in Figure 1. Major component parts of the reactor system included a high purity air cylinder for air supply, a water bath for moisture supply, a thermal chamber for mixing of air and standard substrates, a syringe pump for automatic injection of model toluene and o-xylene gases, gas flowmeters for stream flow rates measurement, a 3-way control valve for sampling gaseous target compounds, and a photoreactor (Pyrex tube with an inner diameter of 3.8 cm and a volume of 133 cm<sup>3</sup>) with an 8 W conventional daylight lamp ( $\lambda = 400\text{--}700$  nm) or 0.32 W white ( $\lambda = 450$  nm) or 0.32 W violet ( $\lambda = 400$  nm) LEDs as a light source. A spinning method was applied for a thin film coating to the inside wall of the Pyrex reactor with each of the prepared photocatalysts. The high-purity air was passed through the water bath for moisture supply at a specified relative humidity. The humidified air was fed into the photocatalytic reactor perpendicularly in order to increase the mass transport of incoming gas to the photocatalyst surface. The representative operating conditions of the photocatalytic reactor system could be described as follows: gas flow rate, 1.0 L min<sup>-1</sup>; relative humidity, 45 ± 5%; input concentration of gaseous target compounds, 0.1 ppm.

Prior to the photodegradation test, the photoreactor was flushed with high-purity air overnight to remove any other chemicals attached to the system. In the absence of catalyst, the reactor was subjected to light irradiation to explore the impact of light on the decomposition of model pollutants. Adsorption equilibrium between the catalyst and the volatile organic compounds was examined by measuring the concentrations of the compounds in input and output airflow. After reaching the adsorption equilibrium (which meant that the input and output concentrations were equal), the light sources were switched on to start the actual photocatalytic tests.

The quantitative analysis of the model pollutants was determined using a gas chromatograph-mass spectrometer (GC-MS; QP2020Ultra, Shimadzu, Kyoto, Japan). During the test, air samples were

collected by drawing air from the sampling ports to Tenax GC-contained stainless steel thermal desorption (TD) tube to concentrate the target compounds. An automatic thermal desorption unit (TD-20, Shimadzu, Japan) was used to transfer sampled compounds to a GC-MS. The adsorbent tube was heat treated, and the chemical species were concentrated on an internal trap. Finally, the internal trap was thermally treated to transport the chemical species to the analytical system.

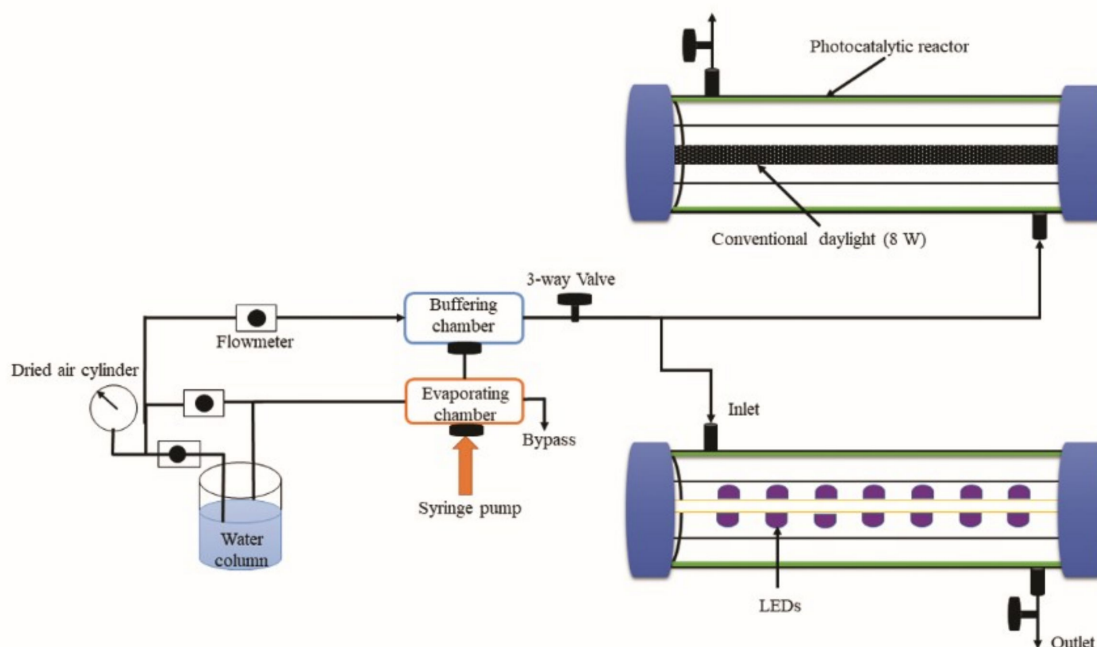


Figure 1. Schematic diagram of photocatalytic reactor system.

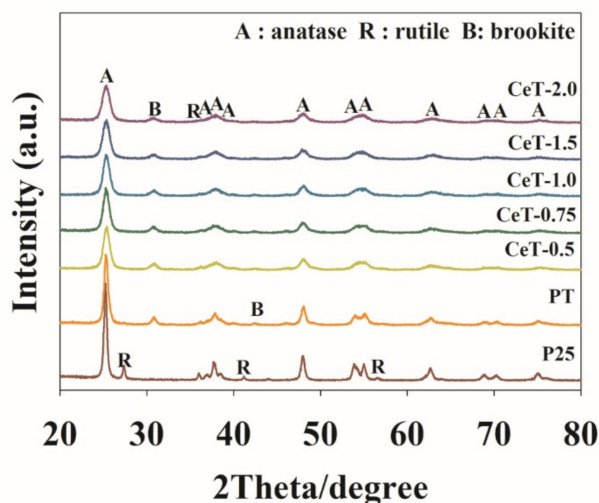
### 3. Results and Discussion

#### 3.1. Characterization of the Fabricated Catalysts

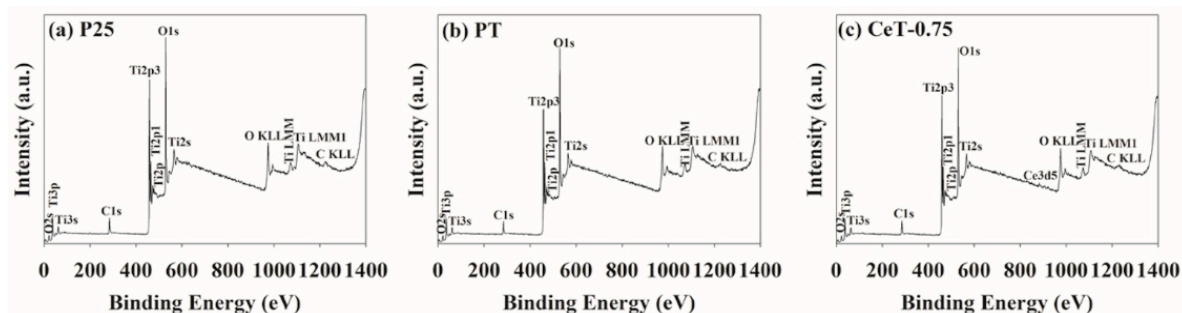
Figure 2 shows the XRD patterns of P25, PT, and Ce-doped  $\text{TiO}_2$  samples synthesized with five different Ce weight ratios (CeT-0.5, CeT-0.75, CeT-1.0, CeT-1.5, and CeT-2.0). All the photocatalysts used in this study revealed anatase, rutile, and brookite phase structures, and anatase phase peak was exhibited as the main structure with a main peak at  $2\theta = 25.3^\circ$ . Feng et al. [38] reported slightly different results than the present work where both PT and CeT exhibited two phase structures of anatase and brookite at ratios of 0.892 and 0.108 in PT and 0.782 and 0.218 in CeT, respectively. The observed difference may have been due to differences in synthesis conditions, including ultrasonic treatment time and amplitude as well as calcination temperature. Rutile phase peaks were shown to be relatively smaller in CeT than in P25. The decreased rutile phase in Ce-doped  $\text{TiO}_2$  photocatalysts was due to the fact that the incorporation of Ce metal ions into  $\text{TiO}_2$  lattice may have impeded the transformation of brookite or anatase to the rutile phase [42]. It is also worth noting that with increase in the weight ratio of Ce in CeT samples, the peak intensities of the anatase phase slightly declined, and the width of the diffraction peaks at  $25.3^\circ$  became broader, clearly indicating the depletion of the crystallization and the decrease of the crystallite sizes [43]. A shift in the diffraction peaks toward higher  $2\theta$  was also noticed for the CeT catalysts, which may have demonstrated the shrinkage of some of the  $\text{TiO}_2$  lattices caused by incorporation of the doped Ce.

As shown in Figure 3, XPS analysis was conducted to survey the surface elements in P25, PT, and CeT-0.75 catalysts. Notably, Figure 3c clearly confirms the successful incorporation of Ce metal ions into the  $\text{TiO}_2$  lattice. The peak at 884 eV was attributed to Ce  $3d_{5/2}$ , which revealed that Ce existed mainly in the +3 oxidation state ( $\text{Ce}^{3+}$ ). The peak intensity of Ce element was very weak due to its low

content. The XPS profiles of P25 and PT (Figure 3a,b) showed the only peaks corresponding to Ti 2p<sub>3/2</sub> (458 eV) and Ti 2p<sub>1/2</sub> (464 eV), and no other peaks related to Ce were observed.



**Figure 2.** XRD spectra of Degussa P25 TiO<sub>2</sub> (P25), pure TiO<sub>2</sub> (PT), and Ce-doped TiO<sub>2</sub> catalysts with different Ce contents (CeT-0.5, 0.75, 1.0, 1.5, and 2.0).



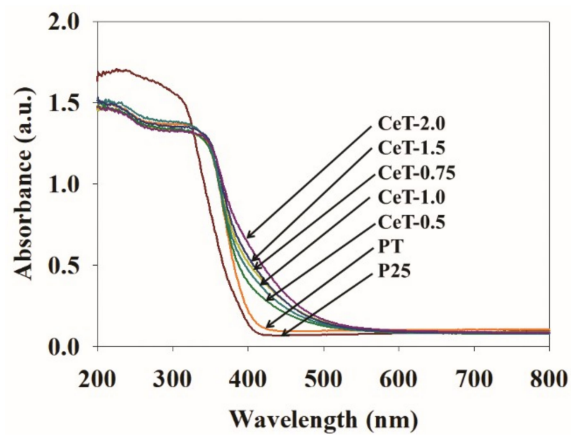
**Figure 3.** X-ray photoelectron spectroscopy (XPS) profiles of (a) Degussa P25 TiO<sub>2</sub> (P25), (b) pure TiO<sub>2</sub> (PT), and (c) Ce-doped TiO<sub>2</sub> (CeT-0.75).

Figure 4 shows the UV-vis DRS patterns of the fabricated photocatalysts. The band-gap energy ( $E_g$ ) of the fabricated samples could be calculated from UV-vis spectroscopy by using the Equation (1):

$$E_g = 1240/\lambda, \quad (1)$$

where  $\lambda$  is the wavelength (nm). Commercial Degussa P25 TiO<sub>2</sub> and pure TiO<sub>2</sub> exhibited a sharp absorbance edge at about 387 nm (3.20 eV) and 398 nm (3.11 eV) and a relatively higher absorbance in the UV region than the other synthesized photocatalysts with no significant absorbance in visible range. This result may have been due to the high rutile phase ratio in P25, as shown in Figure 2. Moreover, the band gaps of P25 and PT were significantly different. It is usually due to the differences in particle size or agglomeration state [44]. Nevertheless, the absorbance edge of all Ce-doped TiO<sub>2</sub> samples with different Ce weight ratios (CeT-0.5, CeT-0.75, CeT-1.0, CeT-1.5, and CeT-2.0) shifted toward the visible region. This result was in accordance with the previous report [38]. Moreover, the shift of the absorbance edge to the visible-light region increased gradually with the increase in Ce weight ratio of 0.5–2.0 wt. %. The band gap energies of CeT-0.5, CeT-0.75, CeT-1.0, CeT-1.5, and CeT-2.0 samples estimated from their absorbance edges were 3.07 eV (404 nm), 3.03 eV (409 nm), 3.00 eV (413 nm), 2.97 eV (417 nm), and 2.89 eV (429 nm), respectively. The extended absorption into the visible range was likely due to the reduction of the band gap resulting from the increased charge transfer owing to the impurity levels that formed in the TiO<sub>2</sub> band structure by doped Ce metal ions [25,45]. From these

results, it was inferred that the Ce-doped TiO<sub>2</sub> photocatalyst could be activated effectively under daylight irradiation.



**Figure 4.** UV-vis diffuse reflectance spectroscopy (UV-vis DRS) of Degussa P25 TiO<sub>2</sub> (P25), pure TiO<sub>2</sub> (PT), and Ce-doped TiO<sub>2</sub> catalysts with different Ce contents (CeT-0.5, 0.75, 1.0, 1.5, and 2.0).

The FE-TEM images revealed the morphologies and sizes of the selected photocatalysts (i.e., P25, PT, and CeT-0.75), as shown in Figure 5. The images of P25 and PT showed lattice fringes of TiO<sub>2</sub> with interplanar spacings of 0.36 and 0.317 nm, respectively. On the other hand, CeT-0.75 exhibited the lattice fringes of TiO<sub>2</sub> and Ce with interplanar spacings of 0.314 and 0.222 nm, respectively. In addition, the elemental mapping images of PT and CeT-0.75 (Figure 6) showed that CeT-0.75 contained Ti, O, and Ce, while PT consisted only of Ti and O. These results indicated that the Ce metal was successfully embedded into the TiO<sub>2</sub> nanostructures during the synthesis of the CeT photocatalysts.

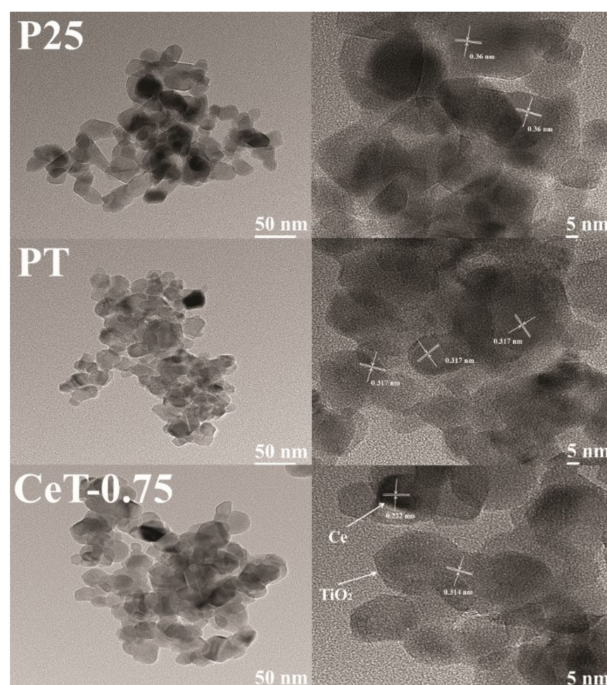


**Figure 5.** TEM and high-resolution TEM images of Degussa P25 TiO<sub>2</sub> (P25), pure TiO<sub>2</sub> (PT), and Ce-doped TiO<sub>2</sub> (CeT-0.75).

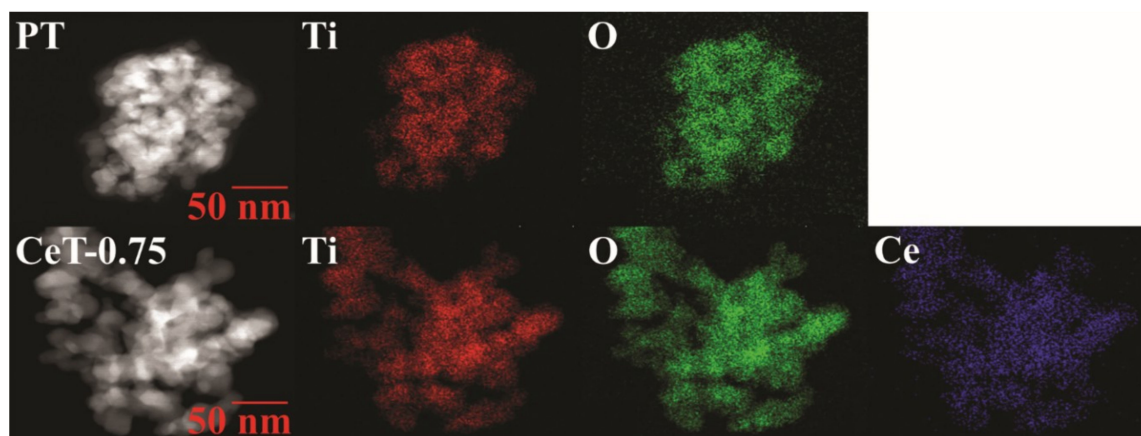


**Figure 6.** Elemental mapping images of pure TiO<sub>2</sub> (PT) and Ce-doped TiO<sub>2</sub> (CeT-0.75) nanostructures.

The average particle sizes of P25, PT, and CeT-0.75 were 24.6 nm, 22.5 nm, and 13.2 nm, respectively, and the other CeT photocatalysts with Ce contents were in the particle size range of 13.6 to 15.3 nm (Table 1). The average particle size was determined using the following Equation (2), assuming all particles to have the same spherical shape and size [46].

$$D = 6000/(S_{\text{BET}} \times \rho) \quad (2)$$

where  $D$  is the particle size,  $S_{\text{BET}}$  is the Brunauer-Emmett-Teller (BET)-specific surface area, and  $\rho$  is the true density ( $\rho$  for titania is 4.2 g mL<sup>-1</sup>).

**Table 1.** Properties of Degussa P25 TiO<sub>2</sub> (P25), pure TiO<sub>2</sub> (PT), and Ce-doped TiO<sub>2</sub> catalysts with different Ce contents (CeT-0.5, 0.75, 1.0, 1.5, and 2.0).

Photocatalyst	$S_{\text{BET}}$ (m <sup>2</sup> g <sup>-1</sup> )	Total Pore Volume (cm <sup>3</sup> g <sup>-1</sup> )	Particle Size (nm)	Crystallite Size of Anatase (nm)	Band Gap, $E_g$ (eV)
P25	58.1	0.198	24.6	24.2	3.20
PT	63.5	0.212	22.5	16.4	3.11
CeT-0.5	96.7	0.312	14.8	12.4	3.07
CeT-0.75	108.6	0.314	13.2	10.9	3.03
CeT-1.0	104.7	0.312	13.6	11.7	3.00
CeT-1.5	94.5	0.309	15.1	12.7	2.97
CeT-2.0	93.5	0.310	15.3	12.8	2.89

The CeT-0.75 sample showed the smallest particle size, whereas the commercial P25 showed the largest particle size. Specific surface areas and total pore volumes of the synthesized photocatalysts were also measured, and the results are summarized in Table 1. The CeT-0.75 exhibited the largest surface area of 108.6 m<sup>2</sup> g<sup>-1</sup> and pore volume of 0.314 cm<sup>3</sup> g<sup>-1</sup>, while the P25 exhibited the lowest values of 58.1 m<sup>2</sup> g<sup>-1</sup> and 0.198 cm<sup>3</sup> g<sup>-1</sup>, respectively, in contrast with the results of particle sizes. Additionally, the specific surface areas of all the synthesized CeT photocatalysts were greater than that of pure TiO<sub>2</sub>, and the surface area values were in the order of CeT-0.75 > CeT-1.0 > CeT-0.5 > CeT-1.5 > CeT-2.0. From the results, it could be concluded that the Ce weight ratio of 0.75 wt. % was the optimum catalyst synthesized under the present experimental conditions.

### 3.2. Photocatalytic Performace

The photocatalytic activities of the synthesized photocatalysts were investigated by determining the decomposition efficiencies for toluene and o-xylene under daylight irradiation. Adsorption equilibrium between the catalysts and the target toluene and o-xylene pollutants was achieved within 2 h after injecting the gases. Figure 7 displays the photodegradation efficiencies for toluene and

o-xylene using P25, PT, and CeT with five different Ce loadings over a 3-h photocatalytic reaction. Over a 3-h photocatalytic reaction, the photocatalytic degradation of the target compounds was almost completed within an initial 1 h, and then there was no noticeable increase in the degradation efficiencies. The degradation efficiencies for the target compounds via CeT photocatalysts were higher than those achieved for P25 and PT. Notably, it was observed that the decomposition efficiencies using CeT photocatalysts increased remarkably in the case of o-xylene compared to toluene. The average decomposition efficiencies for toluene and o-xylene via commercial P25 were 8.1% and 8.5%, respectively. Meanwhile, little increased efficiencies of 11.6% (for toluene) and 41.4% (for o-xylene) were shown in the use of PT. The corresponding degradation efficiencies of five CeT samples (i.e., CeT-0.5, CeT-0.75, CeT-1.0, CeT-1.5, and CeT-2.0) were 35.4%, 49.1%, 44.9%, 30.4%, and 19.4% for toluene and 89.7%, 99.4%, 95.3%, 87.6%, and 81.5% for o-xylene, respectively. It was worth noting that the photocatalytic degradation efficiencies for both target compounds via CeT photocatalysts were determined in the order of CeT-0.75 > CeT-1.0 > CeT-0.5 > CeT-1.5 > CeT-2.0. These results were in agreement with the order of surface area, particle size, and crystallite size of anatase of the five synthesized CeT photocatalysts, as shown in Table 1. Although CeT-0.75 showed less redshift in its light absorption (Figure 4) and wider band gap (Table 1) than CeT-1.5 and CeT-2.0, it yielded the highest photocatalytic reactivity among the prepared photocatalysts, likely because of its increased adsorption capacity. Consequently, it could be described that the photodegradation reactivity of the synthesized photocatalyst was more strongly influenced by its particle size and surface area rather than the redshift or the band gap [38].

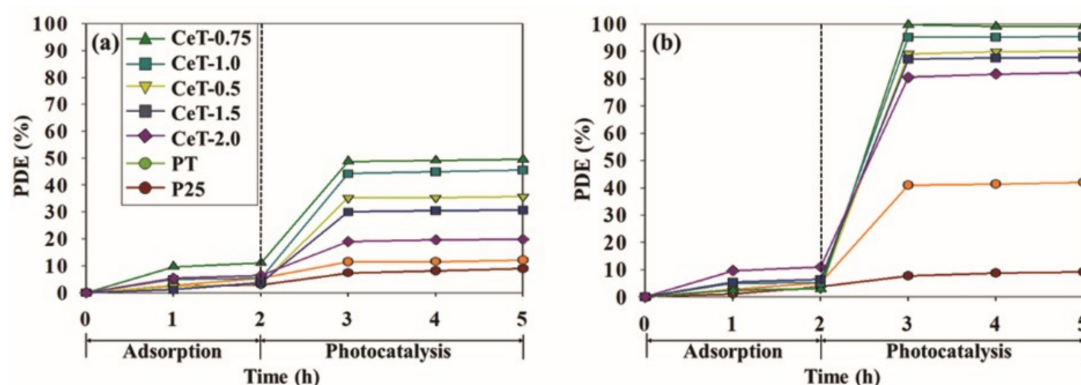


**Figure 7.** Photocatalytic decomposition efficiencies (PDE, %) for (a) toluene and (b) o-xylene determined with Degussa P25 TiO<sub>2</sub> (P25), pure TiO<sub>2</sub> (PT), and Ce-doped TiO<sub>2</sub> catalysts with different Ce contents (CeT-0.5, 0.75, 1.0, 1.5, and 2.0).

The kinetic analysis for the removal of toluene and o-xylene by means of adsorption and photocatalytic degradation was conducted, and the results are shown in Table 2. The following reaction rate equation (Equation (3)) was used for the kinetic analysis:

$$dC/dt = -kC^n \quad (3)$$

where  $C$  is the concentration of target compounds ( $\mu\text{g L}^{-1}$ ),  $t$  is reaction time (h),  $k$  is a reaction rate constant, and  $n$  is the order of reaction. Overall, both the adsorption step and the photocatalytic degradation step were found to be well fitted to the pseudo-second-order kinetic model. In the adsorption step, CeT-0.75 in the case of toluene ( $k_2 = 0.1639 \text{ L } \mu\text{g}^{-1} \text{ h}^{-1}$ ) and CeT-2.0 in the case of o-xylene ( $k_2 = 0.1424 \text{ L } \mu\text{g}^{-1} \text{ h}^{-1}$ ) showed the highest reaction rate constant values in this study. In the subsequent photocatalytic degradation, CeT-0.75 showed a much higher reaction rate constant in decomposition of both toluene ( $k_2 = 0.9227 \text{ L } \mu\text{g}^{-1} \text{ h}^{-1}$ ) and o-xylene ( $k_2 = 99.755 \text{ L } \mu\text{g}^{-1} \text{ h}^{-1}$ ), indicating that CeT-0.75 was the most reactive among the photocatalysts used in this study.

**Table 2.** Kinetic parameters of adsorption and photodegradation of toluene and o-xylene using Degussa P25 TiO<sub>2</sub> (P25), pure TiO<sub>2</sub> (PT), and Ce-doped TiO<sub>2</sub> nanoparticles (CeT-0.5, 0.75, 1.0, 1.5, and 2.0).

Kinetic Model		Pseudo-First-Order Kinetic Model				Pseudo-Second-Order Kinetic Model			
Target Compound		Toluene		o-Xylene		Toluene		o-Xylene	
Parameter		$k_1$ (h <sup>-1</sup> )	R <sup>2</sup>	$k_1$ (h <sup>-1</sup> )	R <sup>2</sup>	$k_2$ (L μg <sup>-1</sup> h <sup>-1</sup> )	R <sup>2</sup>	$k_2$ (L μg <sup>-1</sup> h <sup>-1</sup> )	R <sup>2</sup>
Adsorption step	P25	0.0147	0.8524	0.0189	0.9461	0.0396	0.8537	0.0443	0.9442
	PT	0.0272	1.0000	0.0272	1.0000	0.0742	1.0000	0.0645	1.0000
	CeT-0.5	0.0168	0.9525	0.0168	0.9525	0.0453	0.9542	0.0393	0.9542
	CeT-0.75	0.0583	0.8484	0.0147	0.8524	0.1639	0.8532	0.0344	0.8537
	CeT-1.0	0.0272	0.7934	0.0272	0.7934	0.0742	0.7945	0.0645	0.7945
	CeT-1.5	0.0189	0.9461	0.0331	0.8669	0.0510	0.9442	0.0788	0.8700
	CeT-2.0	0.0331	0.8669	0.0583	0.8484	0.0907	0.8700	0.1424	0.8532
Photocatalytic degradation step	P25	0.0326	0.9447	0.0338	0.9167	0.0905	0.9466	0.0816	0.9178
	PT	0.0453	0.9159	0.1937	0.9045	0.1280	0.9173	0.5925	0.9078
	CeT-0.5	0.1573	0.9003	0.8274	0.8998	0.5241	0.9020	7.5242	0.9101
	CeT-0.75	0.2429	0.8975	1.7160	0.9057	0.9227	0.8992	99.755	0.9475
	CeT-1.0	0.2160	0.9024	1.0981	0.8966	0.7871	0.9055	16.990	0.9046
	CeT-1.5	0.1304	0.8950	0.7508	0.8949	0.4173	0.8954	5.9113	0.8978
	CeT-2.0	0.0786	0.8989	0.6144	0.9014	0.2333	0.8995	3.7749	0.9103

A summary of numerous metal-doped TiO<sub>2</sub> catalysts applied in photocatalytic elimination of toluene and o-xylene are provided in Table 3, which also compares the photocatalytic decomposition efficiency between bare TiO<sub>2</sub> and metal-doped TiO<sub>2</sub>. Comprehensively, dopants could enhance the performance of bare TiO<sub>2</sub> in the decomposition of VOCs (volatile organic compounds) under visible light illumination. They narrowed the band gap of TiO<sub>2</sub> by shifting the light absorption wavelength of TiO<sub>2</sub> from the UV region to the visible region.

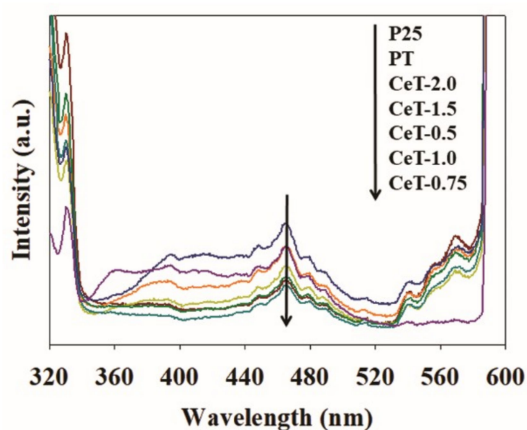
**Table 3.** Comparison of the photodegradation efficiencies of VOCs (volatile organic compounds) with literature values.

Dopant	Doped TiO <sub>2</sub> Preparation Method	Target Compounds	Initial Pollutant Concentration (ppm)	Light Sources	Photocatalytic Degradation Efficiency (%)		Ref.
					Doped TiO <sub>2</sub>	Pure TiO <sub>2</sub>	
Fe W V	Solvothermal method	Toluene	1000–1200	Visible light	48 54 69	20	[47]
Fe	Electrospinning method	Benzene, Toluene, Ethylbenzene, and o-Xylene	0.1	Visible light	68 (toluene) and 91 (o-xylene)	35 (toluene) and 58 (o-xylene)	[48]
Ce	Sonochemical method	Toluene and o-Xylene	0.1	Visible light	49 (toluene) and 99.4 (o-xylene)	11.6 (toluene) and 41.4 (o-xylene)	This study

According to the earlier reports, doping of TiO<sub>2</sub> with metal ions such as Cr, Cu, Fe, Mn, and Zn has enhanced photocatalytic performance for the elimination of environmental contaminants [49–52]. Some other research groups reported that dual-doped TiO<sub>2</sub> nanoparticles with non-metal (N) and metal ion (Fe) showed higher performance than those of N doped or pure TiO<sub>2</sub> on the degradation of 2,4-dichlorophenol and methylene blue under visible light exposure [53,54].

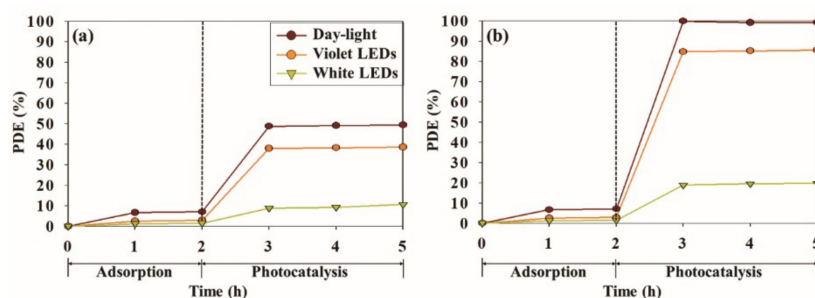
It is well known that the improved photocatalytic performance of the metal-ion doped TiO<sub>2</sub> is most likely due to three main factors: (1) adsorption capacity, (2) separation of charge carriers, and (3) tuning of band gap [45]. The band gaps of the CeT photocatalysts (2.89–3.07 eV) were lower than those of P25 (3.20 eV) and PT (3.11 eV), as shown in Table 1.

The band gap narrowing was ascribed to the metal incorporation that created new electronic states in the band structure, allowing enhanced photocatalytic performances under visible light irradiation. Moreover, the embedded metal ions could capture the electrons, the enhancement of interfacial charge transfer, and the reduction of the recombination of photoexcited charge carriers. The embedded metal elements into the TiO<sub>2</sub> photocatalyst would also improve the separation of photoexcited electron-hole pairs. This was supported by the PL spectra (Figure 8), which displayed weak PL emission intensities of CeT photocatalysts compared to those of P25 and PT. This clearly suggested that the separation efficiencies of the CeT catalysts were higher than those of the P25 and PT samples, since the PL emission intensity was proportional to the recombination of charge carriers [55]. The PL emission intensities of the CeT samples were also determined in the order of CeT-2.0 > CeT-1.5 > CeT-0.5 > CeT-1.0 > CeT-0.75, indicating that the CeT-0.75 had the weakest PL emission intensity among all the catalysts studied (Figure 8).



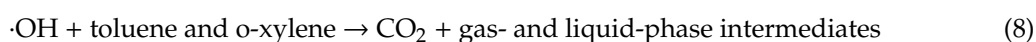
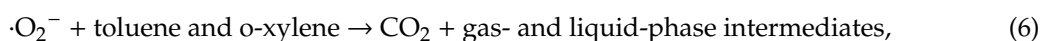
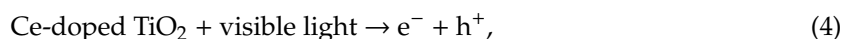
**Figure 8.** Photoluminescence spectroscopy (PL) profiles of Degussa P25 TiO<sub>2</sub> (P25), pure TiO<sub>2</sub> (PT), and Ce-doped TiO<sub>2</sub> catalysts with different Ce contents (CeT-0.5, 0.75, 1.0, 1.5, and 2.0).

Figure 9 depicts the photodecomposition efficiencies for toluene and o-xylene using the CeT-0.75 photocatalyst with the three types of light sources—the 8 W conventional daylight lamp, the 0.32 W white LEDs, and the 0.32 W violet LEDs. After achieving the adsorption equilibrium between the CeT-0.75 catalyst and the target compounds in a dark condition over 2 h, the light irradiation started for the photocatalytic reaction between the photocatalyst and the target chemicals. Over a 3-h photocatalytic reaction, the photocatalytic degradation efficiencies increased within an initial 1 h, and then no conspicuous increment in the degradation efficiencies was shown. In addition, the decomposition efficiencies for o-xylene were evaluated as relatively high compared to those for toluene. The average photodecomposition efficiencies for toluene and o-xylene with the CeT-0.75 photocatalyst according to the light sources were shown in the order of conventional daylight lamp > violet LEDs > white LEDs: 49.1 and 99.4% for conventional daylight lamp, respectively; 40.0 and 85.1% for violet LEDs, respectively; 9.2 and 19.4% for white LEDs, respectively. However, the photodecomposition efficiencies normalized to supplied electric powers were estimated to be in the order of violet LEDs > white LEDs > conventional daylight lamp: 1.25 and 2.66%/W for violet LEDs, respectively; 0.28 and 0.60%/W for white LEDs, respectively; 0.06 and 0.12%/W for conventional daylight lamp, respectively. From these results, it could be interred that the 0.32 W LEDs were much more energy-efficient light sources than the 8 W conventional daylight lamp for the photodecomposition of toluene and o-xylene with the CeT-0.75 photocatalyst, although the photocatalytic reactivity was shown to be higher under the daylight irradiation.



**Figure 9.** Photocatalytic decomposition efficiencies (PDE, %) for (a) toluene and (b) o-xylene determined with CeT-0.75 under three types of light sources (conventional daylight lamp, violet light emitting diodes (LEDs), and white LEDs).

A possible photocatalytic mechanism for the degradation of various organic compounds using metal-doped TiO<sub>2</sub> catalysts was described in previous studies [38,42]. Under light irradiation onto the metal-doped TiO<sub>2</sub> catalysts, a photoexcited electron was transferred from the valence band of TiO<sub>2</sub> to newly created electronic states in the band structure by metals incorporated into the TiO<sub>2</sub> lattice [18,22,23]. Subsequently, the transferred electron reacted with an oxygen molecule (O<sub>2</sub>) to generate a superoxide radical anion ( $\cdot\text{O}_2^-$ ), and the positive hole in the valence band of the TiO<sub>2</sub> reacted with a hydroxyl ion (OH<sup>-</sup>) or a water molecule (H<sub>2</sub>O) to form a hydroxyl radical ( $\cdot\text{OH}$ ). After that, the reactive  $\cdot\text{O}_2^-$  and  $\cdot\text{OH}$  could oxidize the target organic compounds to generate CO<sub>2</sub>, CO, and other byproducts. Consequently, the enhanced performance of the Ce-doped TiO<sub>2</sub> photocatalyst for the photodecomposition of toluene and o-xylene under the visible-light illumination could also be ascribed to the above-mentioned reaction mechanism. In this study, according to Lee and Jo [41], the reaction mechanism could be modified as follows:



#### 4. Conclusions

Ce-doped TiO<sub>2</sub> nanostructures were successfully fabricated by a simplified sonochemical process that could extend the absorbance spectra to a visible range and reduce the frequency of the recombination of photoexcited charge carriers. It was also found that the amount of Ce doping could influence the morphology and the surface properties of the prepared samples, such as particle size, specific surface area, and crystallite size of anatase. The Ce weight ratio of 0.75% was the optimal Ce doping amount in this study. Compared with bare TiO<sub>2</sub> and commercial P25 TiO<sub>2</sub>, the photocatalytic performance of the prepared Ce-doped TiO<sub>2</sub> for the decomposition of toluene and o-xylene under daylight illumination was obviously improved. In particular, the photocatalytic degradation efficiencies by the prepared Ce-doped TiO<sub>2</sub> increased conspicuously in the case of o-xylene compared to the toluene. The degradation efficiencies by the Ce-doped TiO<sub>2</sub> samples were shown in the order of CeT-0.75 > CeT-1.0 > CeT-0.5 > CeT-1.5 > CeT-2.0, in agreement with the order of the surface area and the particle size of the samples. While a conventional daylight lamp showed the highest decomposition efficiency among the used three types of light sources, violet LEDs could be a far more energy efficient light source for the photodecomposition of toluene and o-xylene by CeT-0.75. Consequently, it could be concluded that Ce-doped TiO<sub>2</sub> nanostructures synthesized via a simplified sonochemical process

might have good potential for application in the control of indoor air pollutants since they showed an efficient visible light photoactivity in the decomposition of gaseous toluene and o-xylene.

**Author Contributions:** J.Y.L. and J.-H.C. conceived, designed, and performed the experiments; J.Y.L. and J.-H.C. analyzed the data.

**Funding:** This work was supported by the National Research Foundation of Korea (NRF) grant funded by the Korea government (Ministry of Science and ICT) (NRF-2017R1C1B2002709).

**Conflicts of Interest:** The authors declare no conflict of interest.

## References

1. Shin, S.H.; Jo, W.K. Longitudinal variations in indoor VOC concentrations after moving into new apartments and indoor source characterization. *Environ. Sci. Pollut. Res.* **2013**, *20*, 3696–3707. [[CrossRef](#)] [[PubMed](#)]
2. Ramírez, N.; Cuadras, A.; Rovira, E.; Borrull, F.; Marcé, R.M. Chronic risk assessment of exposure to volatile organic compounds in the atmosphere near the largest Mediterranean industrial site. *Environ. Int.* **2012**, *39*, 200–209. [[CrossRef](#)]
3. Shin, H.T.; Yu, C.L.; Wu, M.T.; Liu, C.S.; Tsai, C.H.; Hung, D.Z.; Wu, C.S.; Kuo, H.W. Subclinical abnormalities in workers with continuous low-level toluene exposure. *Toxicol. Ind. Health* **2011**, *27*, 691–699.
4. Jiménez-Garza, O.; Márquez-Gamiño, S.; Albores, A.; Caudillo-Cisneros, C.; Carrieri, M.; Bartolucci, G.B.; Manno, M. CYP2E1 phenotype in Mexican workers occupationally exposed to low levels of toluene. *Toxicol. Lett.* **2012**, *210*, 254–263. [[CrossRef](#)]
5. Kandyala, R.; Raghavendra, S.P.; Rajasekharan, S.T. Xylene: An overview of its health hazards and preventive measures. *J. Oral Maxillofac. Pathol.* **2010**, *14*, 1–5. [[CrossRef](#)] [[PubMed](#)]
6. Destailats, H.; Sleiman, M.; Sullivan, D.P.; Jacquiod, C.; Sablayrolles, J.; Molins, L. Key parameters influencing the performance of photocatalytic oxidation (PCO) air purification under realistic indoor conditions. *Appl. Catal. B* **2012**, *128*, 159–170. [[CrossRef](#)]
7. Nakata, K.; Fujishima, A. TiO<sub>2</sub> photocatalysis: Design and applications. *J. Photochem. Photobiol. C* **2012**, *3*, 169–189. [[CrossRef](#)]
8. Lai, W.W.P.; Lin, H.H.H.; Lin, A.Y.C. TiO<sub>2</sub> photocatalytic degradation and transformation of oxazaphosphorine drugs in an aqueous environment. *J. Hazard. Mater.* **2015**, *287*, 133–141. [[CrossRef](#)]
9. Chen, X.; Mao, S.S. Titanium dioxide nanomaterials: Synthesis, properties, modifications, and applications. *Chem. Rev.* **2007**, *107*, 2891–2959. [[CrossRef](#)]
10. Yeung, K.L.; Maira, A.J.; Stolz, J.; Hung, E.; Ho, N.K.C.H.; Wei, A.C.; Soria, J.; Chao, K.J.; Yue, P.L. Ensemble effects in nanostructured TiO<sub>2</sub> used in the gas-phase photooxidation of trichloroethylene. *J. Phys. Chem. B* **2002**, *106*, 4608–4616. [[CrossRef](#)]
11. Yu, T.; Tan, X.; Zhao, L.; Yin, Y.; Chen, P.; Wei, J. Characterization, activity and kinetics of a visible light driven photocatalyst: Cerium and nitrogen co-doped TiO<sub>2</sub> nanoparticles. *Chem. Eng. J.* **2010**, *157*, 86–92. [[CrossRef](#)]
12. Wang, B.; Zhang, G.; Sun, Z.; Zheng, S.; Frost, R.L. A comparative study about the influence of metal ions (Ce, La and V) doping on the solar-light-induced photodegradation toward rhodamine B. *J. Environ. Chem. Eng.* **2015**, *3*, 1444–1451. [[CrossRef](#)]
13. Liu, J.; Han, R.; Zhao, Y.; Wang, H.; Lu, W.; Yu, T.; Zhang, Y. Enhanced photoactivity of V–N codoped TiO<sub>2</sub> derived from a two-step hydrothermal procedure for the degradation of PCP–Na under visible light irradiation. *J. Phys. Chem. C* **2011**, *115*, 4507–4515. [[CrossRef](#)]
14. Jing, L.Q.; Sun, X.J.; Xin, B.F.; Wang, B.; Cai, W.; Fu, H. The preparation and characterization of La doped TiO<sub>2</sub> nanoparticles and their photocatalytic activity. *J. Solid State Chem.* **2004**, *177*, 3375–3382.
15. Sukharev, V.; Kershaw, R. Concerning the role of oxygen in photocatalytic decomposition of salicylic acid in water. *J. Photochem. Photobiol. A* **1996**, *98*, 165–169. [[CrossRef](#)]
16. Reinoso, J.J.; Docio, C.M.Á.; Ramírez, V.Z.; Lozano, J.F.F. Hierarchical nano ZnO-micro TiO<sub>2</sub> composites: High UV protection yield lowering photodegradation in sunscreens. *Ceram. Int.* **2018**, *44*, 2827–2834. [[CrossRef](#)]
17. Jiang, D.; Xu, Y.; Hou, B.; Wu, D.; Sun, Y. Synthesis of visible light-activated TiO<sub>2</sub> photocatalyst via surface organic modification. *J. Solid State Chem.* **2007**, *180*, 1787–1791. [[CrossRef](#)]
18. Rauf, M.A.; Meetani, M.A.; Hisaindee, S. An overview on the photocatalytic degradation of azo dyes in the presence of TiO<sub>2</sub> doped with selective transition metals. *Desalination* **2011**, *276*, 13–27. [[CrossRef](#)]

19. Zhang, X.W.; Lei, L.C. One step preparation of visible-light responsive Fe-TiO<sub>2</sub> coating photocatalysts by MOCVD. *Mater. Lett.* **2008**, *62*, 895–897. [[CrossRef](#)]
20. Zhu, J.F.; Chen, F.; Zhang, J.L.; Chen, H.J.; Anpo, M. Fe<sup>3+</sup>-TiO<sub>2</sub> photocatalysis prepared by combining sol-gel method with hydrothermal treatment and their characterization. *J. Photochem. Photobiol. A* **2006**, *180*, 196–204. [[CrossRef](#)]
21. Kim, D.H.; Lee, K.S.; Kim, Y.S.; Chung, Y.C.; Kim, S.J. Photocatalytic activity of Ni 8 wt.-%-doped TiO<sub>2</sub> photocatalyst synthesized by mechanical alloying under visible light. *J. Am. Ceram. Soc.* **2006**, *89*, 515–518.
22. Pelaez, M.; Nolan, N.T.; Pillai, S.C.; Seery, M.K.; Falaras, P.; Kontos, A.G.; Dunlop, P.S.M.; Hamilton, J.W.J.; Byrne, J.A.; O’Shea, K.; et al. A review on the visible light active titanium dioxide photocatalysts for environmental applications. *Appl. Catal. B* **2012**, *125*, 331–349. [[CrossRef](#)]
23. Wang, W.; Zhang, J.; Chen, F.; He, D.; Anpo, M. Preparation and photocatalytic properties of Fe<sup>3+</sup>-doped Ag@TiO<sub>2</sub> core-shell nanoparticles. *J. Colloid Interface Sci.* **2008**, *323*, 182–186. [[CrossRef](#)]
24. Murakami, N.; Ono, A.; Nakamura, M.; Tsubota, T. Development of a visible-light-responsive rutile rod by site-selective modification of iron (III) ion on {111} exposed crystal faces. *Appl. Catal. B* **2010**, *97*, 115–119. [[CrossRef](#)]
25. Chang, S.-M.; Liu, W. The roles of surface-doped metal ions (V, Mn, Fe, Cu, Ce, and W) in the interfacial behavior of TiO<sub>2</sub> photocatalysts. *Appl. Catal. B* **2014**, *156–157*, 466–475. [[CrossRef](#)]
26. Venieri, D.; Fragggedaki, A.; Kostadima, M.; Chatzisyneon, E.; Binas, V.; Zachopoulos, A.; Kiriakidis, G.; Mantzavinos, D. Solar light and metal-doped TiO<sub>2</sub> to eliminate water-transmitted bacterial pathogens: Photocatalyst characterization and disinfection performance. *Appl. Catal. B* **2014**, *154–155*, 93–101. [[CrossRef](#)]
27. Yan, N.; Zhu, Z.; Zhang, J.; Zhao, Z.; Liu, Q. Preparation and properties of Ce-doped TiO<sub>2</sub> photocatalyst. *Mater. Res. Bull.* **2012**, *47*, 1869–1873. [[CrossRef](#)]
28. Ranjit, K.T.; Willner, I.; Bossmann, S.H.; Braun, A.M. Lanthanide oxide doped titanium dioxide photocatalysts: Effective photocatalysts for the enhanced degradation of salicylic acid and t-cinnamic acid. *J. Catal.* **2001**, *204*, 305–313. [[CrossRef](#)]
29. Chai, Y.; Ding, H.; Zhang, Z.; Xian, Y.; Pan, Z.; Jin, L. Study on photocatalytic oxidation for determination of the low chemical oxygen demand using a nano-TiO<sub>2</sub>-Ce(SO<sub>4</sub>)<sub>2</sub> coexisted system. *Talanta* **2006**, *68*, 610–615. [[CrossRef](#)]
30. Li, F.B.; Li, X.Z.; Hou, M.F.; Cheah, K.W.; Choy, W.C.H. Enhanced photocatalytic activity of Ce<sup>3+</sup>-TiO<sub>2</sub> for 2-mercaptobenzothiazole degradation in aqueous suspension for odour control. *Appl. Catal. A* **2005**, *285*, 181–189. [[CrossRef](#)]
31. Rapsonmanikis, A.; Apostolopoulou, A.; Stathatos, E.; Lianos, P. Cerium-modified TiO<sub>2</sub> nanocrystalline films for visible light photocatalytic activity. *J. Photochem. Photobiol. A* **2014**, *280*, 46–53. [[CrossRef](#)]
32. Prasa, K.; Pinjari, D.V.; Pandit, A.B.; Mhaske, S.T. Phase transformation of nanostructured titanium dioxide from anatase-to-rutile via combined ultrasound assisted sol-gel technique. *Ultrason. Sonochem.* **2010**, *17*, 409–415. [[CrossRef](#)]
33. Cheng, H.; Ma, J.; Qi, L. Hydrothermal preparation of uniform nanosize rutile and anatase particles. *Chem. Mater.* **1995**, *7*, 663–671. [[CrossRef](#)]
34. Oseghe, E.O.; Ofomaja, A.E. Facile microwave synthesis of pine cone derived C-doped TiO<sub>2</sub> for the photodegradation of tetracycline hydrochloride under visible-LED light. *J. Environ. Manag.* **2018**, *223*, 860–867. [[CrossRef](#)]
35. Neppolian, B.; Wang, Q.; Jung, H.; Choi, H. Ultrasonic-assisted sol-gel method of preparation of TiO<sub>2</sub> nano-particles: Characterization, properties and 4-chlorophenol removal application. *Ultrason. Sonochem.* **2008**, *15*, 649–658. [[CrossRef](#)]
36. Anandan, S.; Wu, J.J. Ultrasound assisted synthesis of TiO<sub>2</sub>-WO<sub>3</sub> heterostructures for the catalytic degradation of Tergitol (NP-9) in water. *Ultrason. Sonochem.* **2014**, *21*, 1284–1288. [[CrossRef](#)]
37. Yadav, R.S.; Mishra, P.; Pandey, A.C. Growth mechanism and optical property of ZnO nanoparticles synthesized by sonochemical method. *Ultrason. Sonochem.* **2008**, *15*, 863–868. [[CrossRef](#)]
38. Feng, H.; Yu, L.E.; Zhang, M.-H. Ultrasonic synthesis and photocatalytic performance of metal-ions doped TiO<sub>2</sub> catalysts under solar light irradiation. *Mater. Res. Bull.* **2013**, *48*, 672–681. [[CrossRef](#)]
39. Deosarkar, M.P.; Pawar, S.M.; Bhanvase, B.A. In situ sonochemical synthesis of Fe<sub>3</sub>O<sub>4</sub>-graphene nanocomposite for lithium rechargeable batteries. *Chem. Eng. Process.* **2014**, *83*, 49–55. [[CrossRef](#)]

40. Gedanken, A. Using sonochemistry for the fabrication of nanomaterials. *Ultrason. Sonochem.* **2004**, *11*, 47–55. [[CrossRef](#)]
41. Lee, J.Y.; Jo, W.-K. Three-dimensional TiO<sub>2</sub> structures incorporated with tungsten oxide for treatment of toxic aromatic volatile compounds. *Catalysts* **2017**, *7*, 97. [[CrossRef](#)]
42. Venkatachalam, N.; Palanichamy, M.; Murugesan, V. Sol–gel preparation and characterization of alkaline earth metal doped nano TiO<sub>2</sub>: Efficient photocatalytic degradation of 4-chlorophenol. *J. Mol. Catal. A* **2007**, *273*, 177–185. [[CrossRef](#)]
43. Xia, J.; Jiang, D.; Chen, M.; Li, D.; Zhu, J.; Lu, X.; Yan, C. Preparation and characterization of monodisperse Ce-doped TiO<sub>2</sub> microspheres with visible light photocatalytic activity. *Colloids Surf. A* **2010**, *372*, 107–114. [[CrossRef](#)]
44. Reinoso, J.J.; Leret, P.; Álvarez-Docio, C.M.; del Campo, A.; Fernández, J.F. Enhancement of UV absorption behavior in ZnO–TiO<sub>2</sub> composites. *Bol. Soc. Esp. Cerám. V.* **2016**, *55*, 55–62. [[CrossRef](#)]
45. Lee, J.Y.; Jo, W.-K. Simplified sonochemical preparation of titania embedded with selected metals for purification of benzene and toluene. *Ultrason. Sonochem.* **2016**, *28*, 250–256. [[CrossRef](#)]
46. Raj, K.J.A.; Viswanathan, B. Effect of surface area, pore volume and particle size of P25 titania on the phase transformation of anatase to rutile. *Indian J. Chem.* **2009**, *48*, 1378–1382.
47. Papadimitriou, V.C.; Stefanopoulos, V.G.; Romanias, M.N.; Papagiannakopoulos, P.; Sambani, K.; Tudose, V.; Kiriakidis, G. Determination of photo-catalytic activity of un-doped and Mn-doped TiO<sub>2</sub> anatase powders on acetaldehyde under UV and visible light. *Thin Solid Films* **2011**, *520*, 1195–1201. [[CrossRef](#)]
48. Laokiat, L.; Khemthong, P.; Grisdanurak, N.; Sreearunothai, P.; Pattanasiriwisawa, W.; Klysubun, W. Photocatalytic degradation of benzene, toluene, ethylbenzene, and xylene (BTEX) using transition metal-doped titanium dioxide immobilized on fiberglass cloth. *Korean J. Chem. Eng.* **2012**, *29*, 377–383. [[CrossRef](#)]
49. Chun, H.H.; Lee, J.Y.; Jo, W.K. Photocatalysis of low-concentration gaseous organic pollutants over electrospun iron-doped titanium dioxide nanofibers. *Solid State Sci.* **2013**, *25*, 103–109. [[CrossRef](#)]
50. Luiza, D.d.B.; Andersen, S.L.F.; Berger, C.; José, H.J.; Moreira, R.d.F.P.M. Photocatalytic reduction of nitrate ions in water over metal-modified TiO<sub>2</sub>. *J. Photochem. Photobiol. A* **2012**, *246*, 36–44. [[CrossRef](#)]
51. Wang, S.; Meng, K.K.; Zhao, L.; Jiang, Q.; Lian, J.S. Superhydrophilic Cu-doped TiO<sub>2</sub> thin film for solar-driven photocatalysis. *Ceram. Int.* **2014**, *40*, 5107–5110. [[CrossRef](#)]
52. Sood, S.; Umar, A.; Mehta, S.K.; Kansal, S.K. Highly effective Fe-doped TiO<sub>2</sub> nanoparticles photocatalysts for visible-light driven photocatalytic degradation of toxic organic compounds. *J. Colloid Interface Sci.* **2015**, *450*, 213–223. [[CrossRef](#)]
53. Hu, S.; Li, F.; Fan, Z.; Chang, C.-C. Enhanced photocatalytic activity and stability of nano-scaled TiO<sub>2</sub> co-doped with N and Fe. *Appl. Surf. Sci.* **2011**, *258*, 182–188. [[CrossRef](#)]
54. Kim, T.-H.; Rodríguez-González, V.; Gyawali, G.; Cho, S.-H.; Sekino, T.; Lee, S.-W. Synthesis of solar light responsive Fe, N co-doped TiO<sub>2</sub> photocatalyst by sonochemical method. *Catal. Today* **2013**, *212*, 75–80. [[CrossRef](#)]
55. Singh, R.; Pal, B. Study of excited charge carrier's lifetime for the observed photoluminescence and photocatalytic activity of CdS nanostructures of different shapes. *J. Mole. Catal. A* **2013**, *371*, 77–85. [[CrossRef](#)]

